Available online at www.sciencedirect.com
ScienceDirect
International Journal of Heat and Mass Transfer 50 (2007) 1971–1981
International Journal of HEAT and MASS TRANSFER
www.elsevier.com/locate/ijhmt

Numerical and experimental investigation of pressure drop characteristics during upward boiling two-phase flow of nitrogen

Xiangdong Li, Rongshun Wang *, Rongguo Huang, Yumei Shi

School of Mechanical Engineering, Shanghai Jiaotong University, 800 Dongchuan Road, Shanghai 200240, PR China

Received 16 May 2006; received in revised form 11 August 2006
Available online 11 December 2006

Abstract

The characteristics of overall pressure drop during upward boiling two-phase flow of nitrogen with constant mass flux and varying heat flux are experimentally investigated using a vertical tube with an inner diameter of 6.0 mm and numerically simulated using the two-fluid model with new closure correlations. Comparison of the numerical results against the experimental data shows that prior to the transition point in the curve of pressure drop evolution, the predicted pressure drop is in a satisfactory agreement with the experimental data. The present study demonstrates that both the wall lubrication force modeling and the bubble diameter modeling have significant effect on the pressure drop prediction. Both the theoretical analysis and the experimental evidence suggest that the transition point in the pressure drop evolution curve reflects the bubbly-to-slug flow regime transition.

Keywords: Nitrogen; Boiling two-phase flow; Two-fluid model; Overall pressure drop; Transition point

1. Introduction

Boiling flow of liquid nitrogen (LN_2) can find lots of applications in advanced cooling systems for high-temperature superconductors and high-power electronic elements. When designing and operating these cryogenic cooling systems, the overall pressure drop characteristic of a two-phase flow in the channel is an important consideration. Although numerous publications [1–3] deal with the pressure drop characteristics in boiling flow of water with varying mass flux and constant heat flux, in cryogenic cooling systems, the interest is focused on the pressure drop characteristics at different heat flux but constant mass flux, since in these systems change in power is the main cause leading to pressure drop variation.

In an upward boiling flow, the overall pressure drop consists of three components: the gravitational pressure drop, the frictional and the accelerative pressure drop. With increasing void fraction, the gravitational component decreases due to the lower mixture density, while the frictional and accelerative components increase due to volumetric expansion. The relative magnitudes of the variations decide the direction of pressure drop evolution. As shown in Fig. 1, the authors found in their experimental investigations that the overall pressure drop decreases at first with increasing heat flux. However, when the applied heat flux exceeds a certain value, the overall pressure drop begins to increase. Then, if the heat flux is reduced, the pressure drop backtracks along the evolution curve. Accurate prediction of the transition point in the pressure drop curve is very important, since this point may reflect some changes in the heat transfer mechanisms.

In the present study, the overall pressure drop characteristics were numerically simulated in the frame of the commercial CFD code CFX-4.3, using the two-fluid model where some new closure correlations were included. Then experimental investigations were performed in our laboratory to evaluate the models and the numerical procedure. The predicted pressure drop evolution agrees well with

* Corresponding author. Tel./fax: + 86 21 3420 6055.
E-mail address: rswang@sjtu.edu.cn (R. Wang).

0017-9310/$ - see front matter © 2006 Elsevier Ltd. All rights reserved.
doi:10.1016/j.ijheatmasstransfer.2006.09.036

Nomenclature

A_{kj}	interfacial area concentration (m^{-1})
c_{pl}	specific heat of the liquid phase at constant pressure ($J\,kg^{-1}\,K^{-1}$)
D	inner diameter of the tube (m)
d_b	bubble diameter (m)
g	acceleration due to gravity ($m\,s^{-2}$)
H	enthalpy ($J\,kg^{-1}$)
h_{kj}	interfacial heat transfer coefficient ($W\,m^{-2}\,K^{-1}$)
h_{fg}	the latent heat of evaporation ($J\,kg^{-1}$)
k	turbulent energy ($J\,kg^{-1}$)
Ja	the Jacob number $Ja = \rho_l c_{pl}\,\Delta T/(\rho_v h_{fg})$ (dimensionless)
L	local length of the tube (m)
$\dot{m}_{kj}$	interfacial mass transfer rate per unit volume ($kg\,m^{-3}\,s^{-1}$)
$\vec{n}$	unit vector normal to the wall (dimensionless)
p	absolute pressure (Pa)
Q_{kj}	interfacial heat transfer rate per unit volume ($W\,m^{-3}$)
T	temperature (K)
ΔT_{sub}	liquid subcooling, $\Delta T_{sub} = T_{sat} - T_l$ (K)
$\Delta T_{sub,inlet}$	liquid subcooling at the inlet (K)
$\vec{U}$	velocity vector ($m\,s^{-1}$)
y_w	distance from the wall (m)

Greek symbols

α	volume fraction (dimensionless)
λ	heat conductivity ($W\,m^{-1}\,K^{-1}$)
μ	molecular viscosity (Pa s)
ρ	density ($kg\,m^{-3}$)
σ	surface tension ($N\,m^{-1}$)

Subscripts

j and k	phase denotations
kj	from phase j to phase k
l	the liquid phase
sat	saturated
sub	subcooled
v	the vapor phase

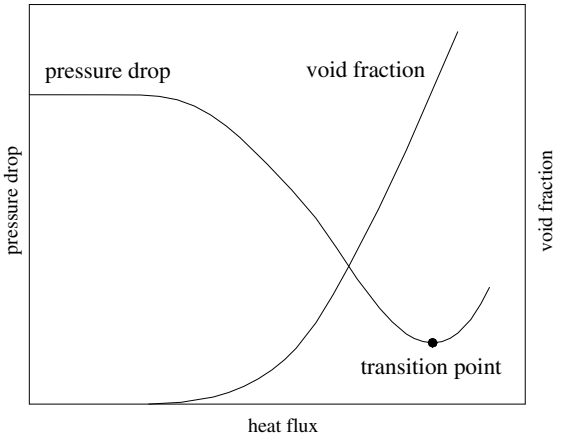

Fig. 1. Characteristics of pressure drop and void fraction evolution.

the experimental data until the transition point. Further study demonstrates that bubbly-to-slug flow regime transition may occur at the transition point, which makes the models proposed in the present study invalid.

Although in a boiling flow channel different flow regimes may appear, bubbly flow is usually expected in these cryogenic cooling systems because of its high efficiency in heat transfer. Therefore, the present study focuses only on bubbly flow and is extended to the transition to slug flow.

2. The two-fluid model for boiling flow of nitrogen

2.1. The conservation equations

In the present study which focuses on nucleate boiling and bubbly flow, the liquid is treated as the continuous phase and the vapor bubbles are treaded as the dispersed phase. The ensemble-averaged conservation equations for each phase are as follows: the continuity equation

$$\frac{\partial}{\partial t}(\alpha_k\rho_k) + \nabla\cdot(\alpha_k\rho_k\vec{U}_k) = \dot{m}_{kj} - \dot{m}_{jk} \tag{1}$$

the momentum equation

$$\frac{\partial}{\partial t}(\alpha_k\rho_k\vec{U}_k) + \nabla\cdot(\alpha_k(\rho_k\vec{U}_k\vec{U}_k - \mu_k^e(\nabla\vec{U}_k + (\nabla\vec{U}_k)^T))) = \alpha_k(\rho_k g - \nabla p_k) + \vec{F}_{kj} + (\dot{m}_{kj}\vec{U}_j - \dot{m}_{jk}\vec{U}_k) \tag{2}$$

and the energy equation

$$\frac{\partial}{\partial t}(\alpha_k\rho_k H_k) + \nabla\cdot(\alpha_k(\rho_k\vec{U}_k H_k - \lambda_k^e\nabla T_k)) = Q_{kj} + (\dot{m}_{kj}H_j - \dot{m}_{jk}H_k) \tag{3}$$

where, the subscripts k and j are phase denotations ($k = l$, $j = v$ or $k = v$, $j = l$). Variables μ_k^e and λ_k^e represent the effective viscosity and conductivity of phase k, respectively. The variables $\dot{m}_{kj}$, F_{kj} and Q_{kj} respectively, represent the transfer rates of mass, momentum and energy per unit volume across the interfaces into phase k from phase j. The terms $\dot{m}_{kj}\bar{U}_j - \dot{m}_{jk}\bar{U}_k$ and $\dot{m}_{kj}H_j - \dot{m}_{jk}H_k$ are included to take into account the additional interfacial transfers of momentum and energy caused by mass transfer.

Since the density of the vapor phase is much lower than that of the liquid phase, it is assumed that the motion of the dispersed vapor bubbles follows the fluctuations in the continuous liquid phase. The vapor phase is assumed as laminar and the turbulence is modeled only for the liquid phase using the $k-\varepsilon$ model. Due to existence of the vapor bub-

bles, the extra turbulence induced by the bubbles in the liquid phase is modeled according to the assumption of Sato [4], where the effective viscosity of the liquid phase is defined by

$$\mu_{\mathrm{l}}^{\mathrm{e}} = \mu_{\mathrm{l}} + C_{\mu}\rho_{\mathrm{l}}\frac{k_{\mathrm{l}}^2}{\varepsilon_{\mathrm{l}}} + C_{\mu\mathrm{b}}d_{\mathrm{b}}\alpha_{\mathrm{v}} \mid \vec{U}_{\mathrm{v}} - \vec{U}_{\mathrm{l}} \mid \tag{4}$$

where, the first term in the right-hand-side of Eq. (4) represents the molecular viscosity of the liquid phase, the second and the third terms are the shear-induced and bubble-induced turbulent viscosity, respectively. The coefficients are $C_{\mu} = 0.09$ and $C_{\mu\mathrm{b}} = 0.6$.

For boiling flow in channels, vapor generation on the heating surface is the source of void in the interior of the flow. The main parameters describing the process of bubble generation and departure include the bubble departure diameter d_{bW}, the bubble departure frequency f, the active site density n, the bubble waiting time t_{w} and the wall area fraction subjected to quenching A_{q}. The authors found in their previous study [5] that the default correlations for wall heat flux partitioning in the CFX code [6], which were originally proposed for nucleate boiling of water, is invalid when modeling boiling flow of LN_2. In the present job, the bubble departure diameter and the active site density are modeled according to Kirichenko [7], the bubble departure frequency is modeled according to Kocamustafaogullari and Ishii [8], the bubble waiting time is modeled according to Bald [9] and the quenching area fraction is modeled according to Kenning [10]. Details of the above correlations have been highlighted elsewhere [5] by the authors and will not be repeated here.

2.2. Momentum transfer across interfaces

The inter-phase momentum transfer is modeled with the interfacial forces. For boiling flow of cryogenic liquids in vertical tubes, the following forces must be taken into account: the drag force $\vec{F}_{\mathrm{D}}$ [11], the lift force $\vec{F}_{\mathrm{L}}$ [12], the turbulent dispersion force $\vec{F}_{\mathrm{TD}}$ [13] and the wall lubrication force $\vec{F}_{\mathrm{W}}$ [14]. The total interfacial force per unit volume is the sum of the above forces.

$$\vec{F}_{\mathrm{lv}} = -\vec{F}_{\mathrm{vl}} = \vec{F}_{\mathrm{D}} + \vec{F}_{\mathrm{L}} + \vec{F}_{\mathrm{TD}} + \vec{F}_{\mathrm{W}} \tag{5}$$

where

$$\vec{F}_{\mathrm{D}} = \frac{3}{4}\frac{C_{\mathrm{D}}}{d_{\mathrm{b}}}\alpha_{\mathrm{v}}\rho_{\mathrm{l}} \mid \vec{U}_{\mathrm{v}} - \vec{U}_{\mathrm{l}} \mid (\vec{U}_{\mathrm{v}} - \vec{U}_{\mathrm{l}}) \tag{6}$$

$$\vec{F}_{\mathrm{L}} = C_{\mathrm{L}}\alpha_{\mathrm{v}}\rho_{\mathrm{l}}(\vec{U}_{\mathrm{v}} - \vec{U}_{\mathrm{l}}) \times (\nabla \times \vec{U}_{\mathrm{l}}) \tag{7}$$

$$\vec{F}_{\mathrm{TD}} = -C_{\mathrm{TD}}\rho_{\mathrm{l}}k_{\mathrm{l}}\nabla\alpha_{\mathrm{l}} \tag{8}$$

$$\vec{F}_{\mathrm{W}} = -\frac{\alpha_{\mathrm{v}}\rho_{\mathrm{l}}(\vec{U}_{\mathrm{v}} - \vec{U}_{\mathrm{l}})^2}{d_{\mathrm{b}}}\max\left(0, C_{\mathrm{W1}} + C_{\mathrm{W2}}\frac{d_{\mathrm{b}}}{y_{\mathrm{W}}}\right)\vec{n} \tag{9}$$

where, the drag coefficient C_{D} is modeled according to Ishii and Zuber [11]. The authors [5] found that for boiling bubbly flow of LN_2 in vertical tubes, the most appropriate lift coefficient is $C_{\mathrm{L}} = 0.1$, which means that the lift force on a vapor bubble acts in the direction of decreasing liquid velocity. The turbulent dispersion coefficient is $C_{\mathrm{TD}} = 0.1$. The coefficient C_{W1} and C_{W2} decide the magnitude of the wall lubrication force and the region in which it exists. In the research community there is no consensus in selecting appropriate C_{W1} and C_{W2} at present. For example, different definitions such as $C_{\mathrm{W1}} = -0.04$, $C_{\mathrm{W2}} = 0.08$ [15], $C_{\mathrm{W1}} = -0.01$, $C_{\mathrm{W2}} = 0.05$ [16], and $C_{\mathrm{W1}} = -0.1$, $C_{\mathrm{W2}} = 0.147$ [17] have appeared in the literature. In the present study, sensitive analyses were performed to find out the most suitable values of C_{W1} and C_{W2}, which will be shown in Section 4.

2.3. Heat and mass transfers across interfaces

In the interior of the flow, it is assumed that the temperature of the vapor phase is constant at the local saturation temperature and heat and mass are transferred across the interfaces. Therefore, it becomes a key issue to estimate the interfacial area per unit volume (known as the interfacial area concentration) since interfacial transfer of momentum, energy and mass are all related to this parameter.

For a bubbly flow, spherical bubbles are assumed and the local interfacial area concentration is defined by

$$A_{\mathrm{lv}} = A_{\mathrm{vl}} = \frac{6\alpha_{\mathrm{v}}}{d_{\mathrm{b}}} \tag{10}$$

where, d_{b} is the local bubble diameter. In the open literature [18,19], the linear assumption of Anglart and Nylund [20] for bubble diameter is widely employed

$$d_{\mathrm{b}} = \begin{cases} d_{\mathrm{b0}} & \Delta T_{\mathrm{sub}} \geqslant \Delta T_{\mathrm{sub,0}} \\ \frac{d_{\mathrm{b1}}(\Delta T_{\mathrm{sub}} - \Delta T_{\mathrm{sub,0}}) + d_{\mathrm{b0}}(\Delta T_{\mathrm{sub,1}} - \Delta T_{\mathrm{sub}})}{\Delta T_{\mathrm{sub,1}} - \Delta T_{\mathrm{sub,0}}} & \Delta T_{\mathrm{sub,0}} > \Delta T_{\mathrm{sub}} > \Delta T_{\mathrm{sub,1}} \\ d_{\mathrm{b1}} & \Delta T_{\mathrm{sub,1}} \geqslant \Delta T_{\mathrm{sub}} \end{cases} \tag{11}$$

where d_{b0} and d_{b1} are user-defined bubble diameters at reference liquid subcoolings $\Delta T_{\mathrm{sub,0}}$ and $\Delta T_{\mathrm{sub,1}}$, respectively. In the present work, the following user-defined bubble diameters are selected: $\Delta T_{\mathrm{sub,0}} = \min(5, \Delta T_{\mathrm{sub,inlet}})$ K, $d_{\mathrm{b0}} = 0.05$ mm and $\Delta T_{\mathrm{sub,1}} = -0.1$ K, $d_{\mathrm{b1}} = d_{\mathrm{b,crit}}$ (defined in Eq. (16)).

For the purpose of comparison, the bubble diameter correlation proposed by Zeitoun and Shoukri [21] is also incorporated

$$d_{\mathrm{bs}} = \frac{0.0683(\rho_{\mathrm{l}}/\rho_{\mathrm{v}})^{1.326}}{Re^{0.324}\left(Ja_{\mathrm{sub}} + \frac{149.2(\rho_{\mathrm{l}}/\rho_{\mathrm{v}})^{1.326}}{Bo^{0.478}Re^{1.6}}\right)}\sqrt{\frac{\sigma}{(\rho_{\mathrm{l}} - \rho_{\mathrm{v}})}} \tag{12}$$

where, d_{bs} is the mean Sauter diameter of the bubbles, σ is the surface tension, Re is the Reynolds number, Bo is the boiling number and Ja_{sub} is the Jacob number related to the liquid subcooling.

The direction and rate of mass transfer in the interior of the flow depends on the liquid temperature. If the liquid is

superheated, there is a bulk evaporation from the liquid to the vapor phase, otherwise, bulk condensation occurs. The mass transfer rate is

$$\dot{m}_{\mathrm{vl}} = \max\left(\frac{h_{\mathrm{vl}}(T_{\mathrm{l}} - T_{\mathrm{sat}})A_{\mathrm{vl}}}{h_{\mathrm{f}g}}, 0\right) \tag{13}$$

or

$$\dot{m}_{\mathrm{lv}} = \max\left(\frac{h_{\mathrm{lv}}(T_{\mathrm{sat}} - T_{\mathrm{l}})A_{\mathrm{lv}}}{h_{\mathrm{fg}}}, 0\right) \tag{14}$$

where, h_{lv} and h_{vl} are the interfacial heat transfer coefficients defined by Ranz and Marshall (cited in [22]).

$$Nu_{kj} = h_{kj}d_{\mathrm{b}}/\lambda_{\mathrm{l}} = 2 + 0.6Re_{\mathrm{b}}^{1/2}Pr_{\mathrm{l}}^{1/3} \tag{15}$$

where, Re_{b} is the bubble Reynolds number ($Re_{\mathrm{b}} = \rho_{\mathrm{l}}|\vec{U}_{\mathrm{v}} - \vec{U}_{\mathrm{l}}|d_{\mathrm{b}}/\mu_{\mathrm{l}}$) and Pr_{l} is the liquid Prandtl number ($Pr_{\mathrm{l}} = \mu_{\mathrm{l}}\, c_{\mathrm{pl}}/\lambda_{\mathrm{l}}$).

3. Description of the experimental facility and procedure

3.1. The experimental rig

As shown in Fig. 2, the experimental rig includes the following main parts: a high-pressure liquid tank, a low-pressure liquid vessel, a subcooler, a test chamber, an evapourizer, an adjustable power system and the measuring and controlling instruments. The high-pressure liquid nitrogen tank, which is made of stainless steel, has a capacity of 2000 l and a maximum working pressure of 3.5 MPa. The working pressure in the tank can be steadily maintained using a pressure control gauge. Downstream of the high-pressure liquid tank, a subcooler is arranged to cool down the liquid from the tank and to ensure the subcooling of the working fluid. The subcooler is made of a coiled pipe with a length of 6.0 m and a Dewar type container with a capacity of 15 l. The coolant of the subcooler is saturated LN_2 at a lower pressure and hence at a lower saturation temperature than in the case of the working fluid in the coiled pipe. The coolant is supplied from the low-pressure liquid vessel, which has a capacity of 175 l. In order to reduce heat leakage from the environment, the working fluid is transported from the high-pressure liquid tank to the subcooler and then to the test chamber using vacuum-insulated flexible cryogenic pipes. The flow rate of the working fluid is measured using a digital mass flowmeter with a measuring range of 0–1000 SLPM (standard liter per minute) and an accuracy of 0.1% after it is vaporized in an industrial evapourizer.

The test chamber is schematically illustrated in Fig. 3, which includes a cryogenic chamber, a cold screen, a vapor–liquid separator, a hydrodynamic–thermodynamic stabilizer and the test section. The cryogenic chamber, which has an inner diameter of 280 mm and a depth of 1300 mm, is made of stainless steel and is thermally insulated using the so-called "super insulation" technique. In order to eliminate heat leakage from the environment to the test section as possible, a circular inner shell with a wall thickness of 3 mm is coaxially installed in the cryogenic chamber. The outer diameter of the shell is 250 mm and the length is 1280 mm. In the jacket layer between the inner shell and the cryogenic chamber, LN_2 is filled to form a cold screen. By this arrangement, the heat leakage from the environment to the test section can be reduced to the minimum. In order to ensure a single-phase flow entering the test section, a vapor–liquid separator is designed. A stabilizer is then installed downstream of the vapor–liquid separator, in which the working fluid reaches steady-state conditions. The remaining space in the inner shell is filled with expanded pearlite particles and is vacuumed to 1×10^{-2} Pa using a vacuum pump.

The structure of the test section and related measuring instruments are shown in Fig. 4. The test section is a circular tube made of 304# stainless steel (0Cr18Ni9), with an inner diameter of 6.0 mm, a wall thickness of 1.0 mm and

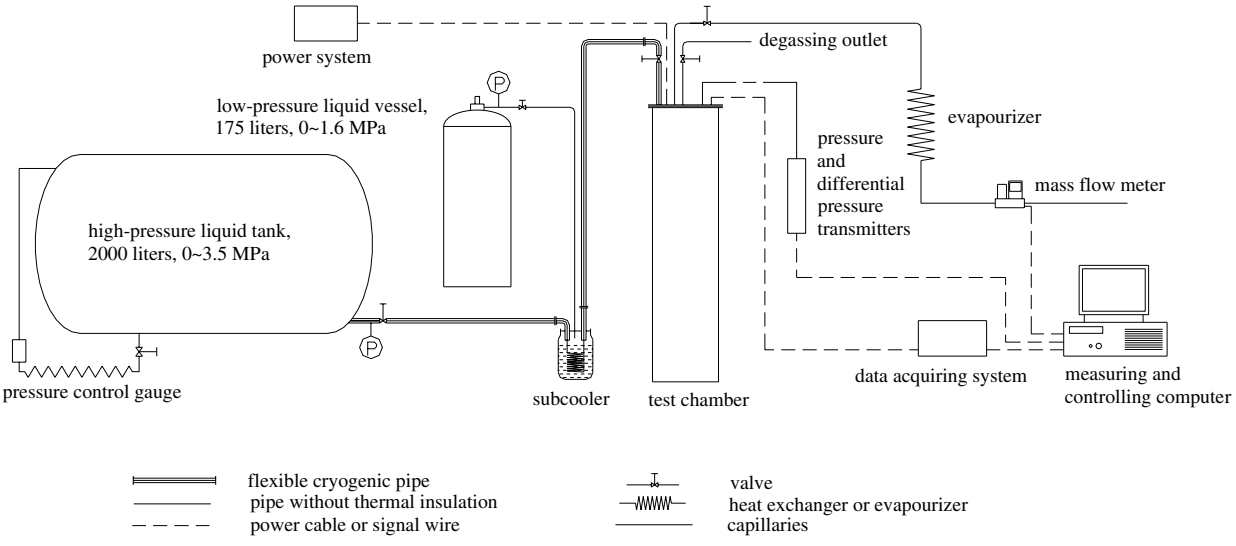

Fig. 2. Schematic diagram of the experimental rig.

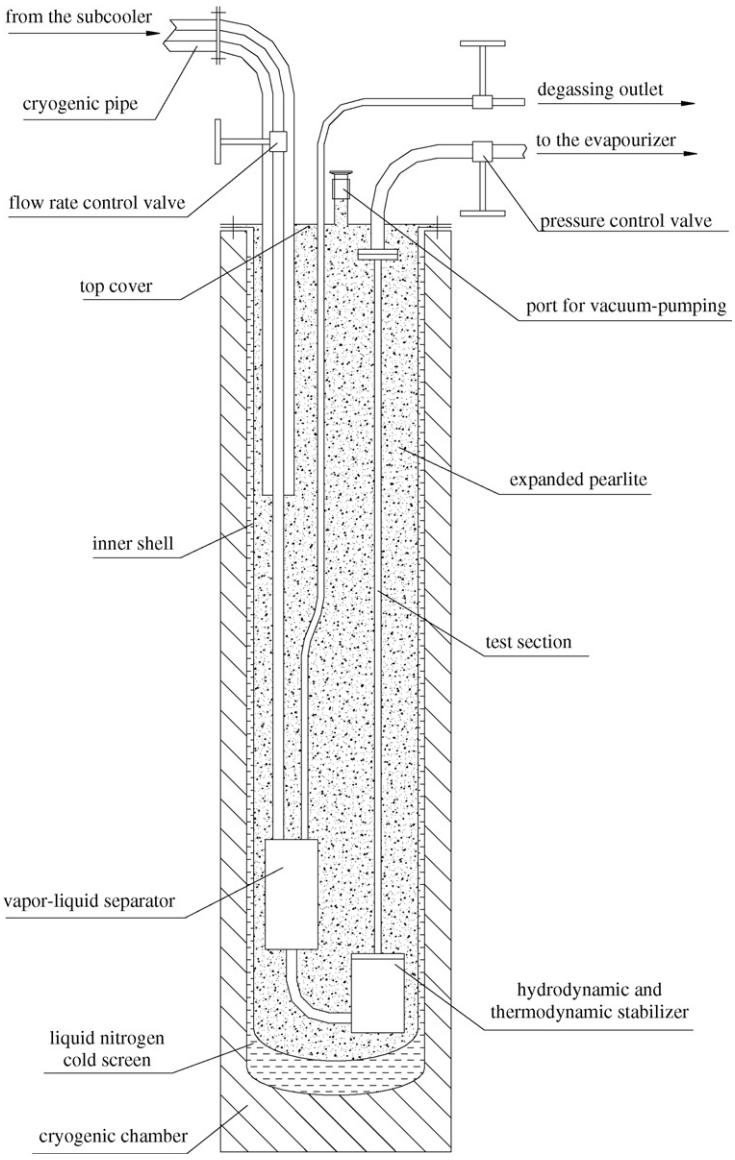

Fig. 3. Schematic diagram of the test chamber.

a length of 1050 mm. The tube is connected to the stabilizer and to the top cover using flanges, with annealed red copper as the sealing material. In the stabilizer, a platinum resistance thermometer with an accuracy of 0.05 K is installed. The pressure in the stabilizer is measured using a pressure transmitter with a measurement range of 0–3.0 MPa and an error of 0.5%. Another pressure transmitter with the same range and accuracy is installed near the outlet of the tube. According to the temperature and pressure in the stabilizer, together with the records of the flowmeter, the thermodynamic properties and the mean velocity of the working fluid entering the test section can be determined. Two capillaries are fixed to the tube near the inlet and the outlet respectively, the heated part is the part of the tube between the capillaries, which has an effective length of 1000 mm. A differential pressure transmitter with a measurement range of 0–30.0 kPa and an error of 0.5% is used to measure the overall pressures drop, the records of which will be used as the benchmark data. Between the two capillaries, heating belt is wrapped around the tube and the applied power is controlled using the adjustable power system.

3.2. Experimental procedure

Before the experiments were performed, LN_2 was filled in the jacket layer and channels in the test chamber and was maintained for about 12 h until a thermally steady condition was built up. Then an experiment with zero heat flux was firstly performed to estimate the heat leakage from the environment to the test section. It is estimated that the heat leakage to the test section is less than 10 W/m^2, which can be neglected compared with the applied heat flux.

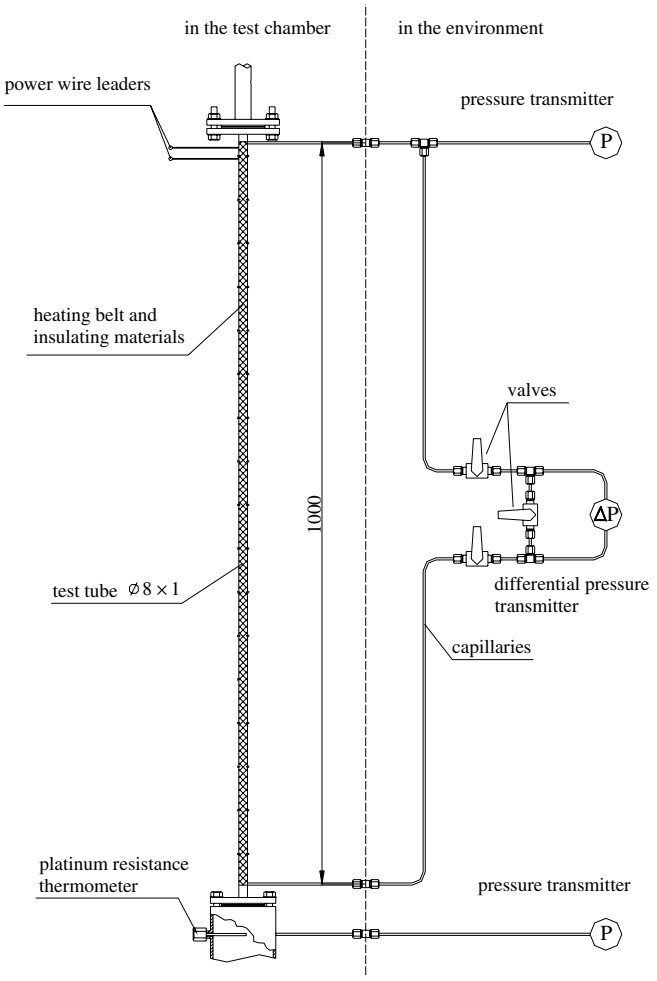

Fig. 4. Schematic diagram of the test section.

Experiments were performed under system pressures of 1.13 and 0.72 MPa respectively, where the system pressure was defined as the absolute pressure averaged from the inlet and outlet pressures. Under each system pressure case, the mass flux was carefully controlled and the heat flux was increased and then reduced step by step. The liquid subcooling at the inlet was jointly decided by the system pressure and the mass flux, larger subcooling appeared at higher system pressure and larger mass flux and vice versa. Due to the inherent instability of two-phase flows, the readings of the instruments kept fluctuating, but the average values of the readings were almost constants. Therefore, signals of the mass flux, pressure, different pressure and temperature were acquired at a sampling frequency of 1.0 Hz for at least 30 min and the time-averaged values were used as the computational conditions and the benchmark data. Details of the experimental data together with the computational boundary conditions are listed in Table 1.

4. Results and discussion

The commercial CFD code CFX-4.3 was used as a frame to perform the computations. The models proposed in the present study were incorporated in the code through the user subroutines. Due to the axial symmetry of the two-phase flow field, a two-dimensional computational domain with a dimension of 3×1000 mm was built and three different grid arrangements (5×1000, 10×1000 and 15×1000 rectangular cells) were tested. The cells in the axial direction have the same size and the radial grid density increases gradually towards the wall. In all grid arrangement cases, the size of the cell near the axis is twice

Table 1
Operating parameters of the experiments and boundary conditions of the computations

Experiments/computations	Experiments	Computations	Experiments	Computations
Outlet pressure (MPa)	1.07 ± 0.05	1.07	0.65 ± 0.05	0.65
Mass flux (kg/(m^{2}s))	585 ± 10	585	185 ± 5	185
Inlet subcooling (K)	10.6 ± 0.3	10.6	2.2 ± 0.2	2.2
Heat flux (kW/m^2)				
1	19.14	18.00	1.54	1.30
2	20.45	20.00	1.66	1.50
3	21.79	21.00	1.86	1.70
4	22.44	22.00	1.95	1.90
5	23.07	23.00	2.04	2.05
6	23.58	24.00	2.12	2.15
7	24.13	25.20	2.16	2.25
8	24.47	26.0	2.21	2.30
9	24.93	26.50	2.26	2.35
10	25.24	26.75	2.29	2.375
11	25.61	27.00	2.32	2.40
12	25.78		2.33	
13	26.06		2.37	
14	26.38		2.40	
15	26.81		2.42	
16	27.12			
17	27.37			

of that of the cell near the wall. It was found that there was no significant difference between the predicted results of the 10×1000 and those of the 15×1000 grid arrangements. Therefore it is confirmed that the 10×1000 grid arrangement is adequate to the issue of the present study.

The discretization of transport equations was based on a conservative finite-volume method. In the computations, the following options and settings were used: a free slip boundary condition for the vapor phase was used at the wall and a logarithmic wall function was used as a wall boundary condition for the liquid phase velocity; uniform velocity and temperature profiles were set at the inlet; a pressure boundary condition was applied at the outlet; a constant heat flux boundary condition was applied at the wall. The experiments showed that the overall pressure drop varies with the heat flux, but it seems that the pressure drop evolves along a fix curve, despite the increasing or decreasing heat flux. Therefore, monotonously increasing heat fluxes were employed in the computations, despite the experimental procedure.

Convergence was achieved within 3000 iterations when the residual of the continuity equation of the liquid phase reduced to be less than 1×10^{-5} kg/s.

4.1. Influence of wall lubrication force

The wall lubrication force acts in the normal direction away from the wall and prevents the accumulation of bubbles near the wall. This force acts only in a region within $|C_{W2}/C_{W1}|$ bubble diameters away from the wall. Therefore, it could be expected that in a large diameter tube, the effect of the wall lubrication force could be neglected, while in a small diameter tube, such as that employed in the present study, which is of an inner radius of 3 mm, the cross-sectional area fraction in which the wall lubrication force exits may be large and its effect may be significant. Even in boiling flow of water, the effect of the wall lubrication force has not been completely investigated. Since no explicit values of C_{W1} and C_{W2} for nitrogen boiling flow are available, sensitive analyses were performed in the present study. In the computations, C_{W1} took a constant value of $C_{W1} = -0.01$ (recommended by the CFX code [6]) and three values of C_{W2} ($C_{W2} = 0.015$, 0.03 and 0.05) were tested. The bubble diameter distribution was modeled using the linear equation of Aglart and Nylund (Eq. (11)), other models and parameters were kept unchanged. With these settings, the wall lubrication force acts in a region within 1.5, 3.0 and 5.0 bubble diameter away from the wall, respectively.

As shown in Fig. 5, modeling of the wall lubrication force has a significant effect on the predicted radial parameter distributions. With larger C_{W2}, the wall lubrication force has a larger magnitude and wider effective region. As a result, the vapor bubbles move at a faster velocity towards the axis of the tube, as shown in Fig. 5(a). Accordingly, as shown in Fig. 5(b), with increasing C_{W2}, the predicted peak of the void fraction moves further towards

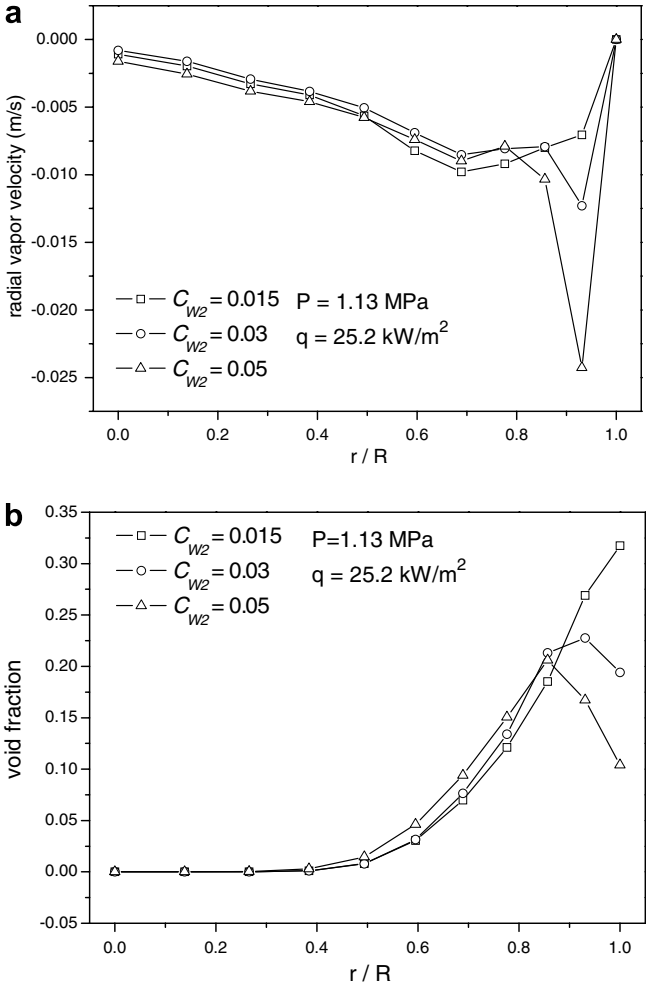

Fig. 5. Radial parameter distributions at $L = 0.8$ m (1.13 MPa) (a) radial vapor velocity and (b) void fraction.

the axis. The computation with $C_{W2} = 0.015$ predicted a monotonously increasing void fraction profile along the radius (Fig. 5(a)). Numerous experimental investigations [23,24] of upward boiling flow of water demonstrated that the radial void fraction profile follows a near-wall peak distribution. Although there is no experimental evidence available, it is reasonable to assume that the void fraction profile in boiling flow of LN_2 follows a similar profile to that in boiling flow of water, since LN_2 has a smaller molecular viscosity than water and nitrogen bubbles can move more easily towards the axis. Therefore, it can be assumed that $C_{W2} = 0.015$ under-predicts the wall lubrication force.

The overall pressure drop evolution with varying heat flux was then predicted using $C_{W2} = 0.03$ and $C_{W2} = 0.05$ respectively, and was compared against the experimental data, as shown in Fig. 6. It seems that the evolution predicted using $C_{W2} = 0.03$ matches the experimental data better. Especially, with $C_{W2} = 0.03$, the predicted heat flux at which the transition occurs coincides with the experimental data, while computation with $C_{W2} = 0.05$ over-predicts this heat flux. It seems according to Fig. 6 that the

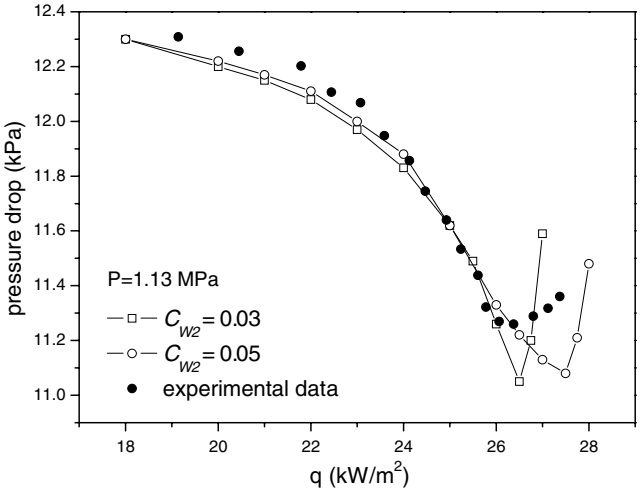

Fig. 6. Influence of the wall lubrication force modeling on pressure drop prediction (1.13 MPa).

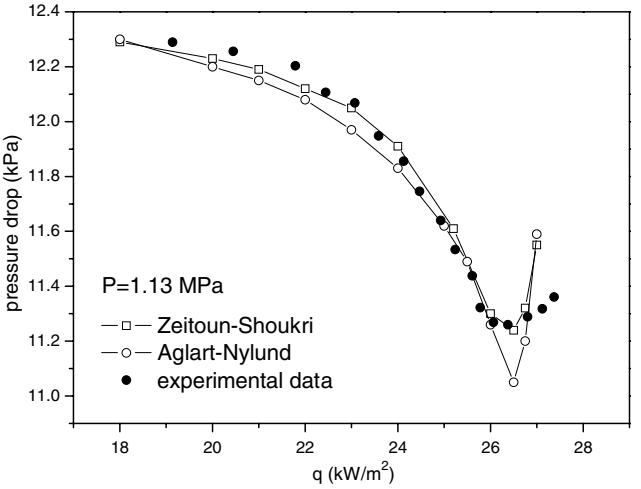

Fig. 8. Influence of bubble diameter modeling on pressure drop prediction (1.13 MPa).

predicted heat flux at the transition point is strongly influenced by the wall lubrication force modeling. In the following computations, $C_{W2} = 0.03$ is employed. However, Fig. 6 also shows that the simulations failed to predict the value of the pressure drop at the transition point. Further study demonstrated that the predicted value of the pressure drop at the transition point is strongly decided by the bubble diameter modeling.

4.2. Influence of bubble diameter

The bubble diameter was modeled using the Anglar–Nylund model (Eq. (11)) and the Zeitoun–Shoukri model (Eq. (12)), respectively, while other models and parameters were kept unchanged. Shown in Fig. 7 is the radial profile of bubble diameter distribution at $L = 0.8$ m. Both the models predict similar radial bubble diameter evolving tendencies, but the Zeitoun–Shoukri model predicts smaller bubble diameters than the Anglar–Nylund model. Evolution of the pressure drop was then predicted using Eqs. (11) and (12) respectively, and was compared against the experimental data, as shown in Fig. 8. It is clear that the Zeitoun–Shoukri model makes a better prediction than the Anglar–Nylund model. Especially, the predicted pressure drop using the former model agrees well with the experimental data when the transition occurs. Although direct evidence is absent, it can be supposed that the bubble diameter in boiling flow of LN_2 follows the Zeitoun–Shoukri model, since the pressure drop characteristics predicted using this model agree well with the experimental data.

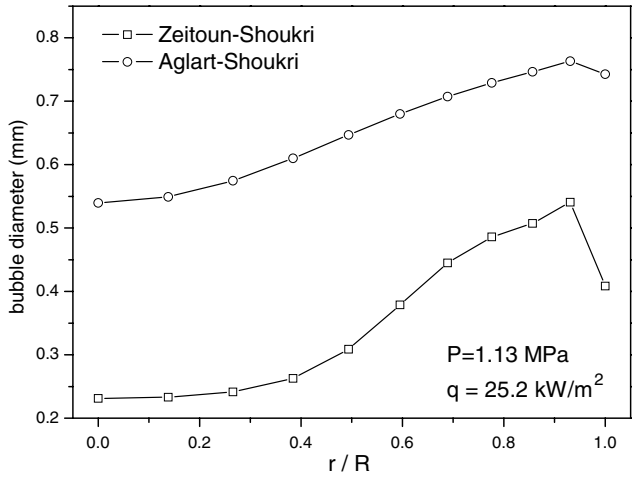

Fig. 7. Radial bubble diameter distribution at $L = 0.8$ m (1.13 MPa).

4.3. Further discussion

As shown in Fig. 8, beyond the transition point, the predicted pressure drop begins to deviate away from the experimental data. It is supposed that the deviation is perhaps due to bubbly-to-slug flow regime transition occurring at the transition point, which leads to that the models for bubbly flow presented in the present study become invalid.

Generally, the bubbly-to-slug flow regime transition criterion is related to the void fraction. However, a generally accepted expression for the void fraction at the transition is still absent. For example, Mishima and Ishii [25] proposed that the transition occur at $\alpha_v = 0.3$ through a geometrical consideration while Taitel [26] supposed $\alpha_v = 0.25$ via experimental investigations. Barnea [27] illustrated that for a bubbly flow, there exists a critical bubble diameter defined by

$$d_{b,crit} = 2\sqrt{\frac{0.4\sigma}{(\rho_l - \rho_v)g}} \tag{16}$$

It is found that bubbles smaller than the critical size remain spherical but those above the critical size are distorted. The spherical and the distorted bubbles may coexist with each other or coalesce and generate Taylor bubbles causing a

transition to slug flow, depending on the tube size [28]. Das and Pattanayak [29,30] experimentally investigated upward two-phase flow of cryogenic liquids and found that if the tube diameter D is such that

$$D < 19.1 \times \sqrt{\frac{(\rho_l - \rho_v)\sigma}{g\rho_l^2}} \tag{17}$$

then, as soon as bubbles above the critical size are formed, they coalesce with others and generate Taylor bubbles instead of forming a bubbly mixture. This means for a nitrogen two-phase flow under system pressure of 1.13 MPa, if the tube diameter is approximately less than 12.6 mm then direct transition from dispersed bubble flow to slug flow is possible. Therefore, it can be expected that for the tube employed in the present study, which is of an inner diameter of 6.0 mm, there is a high tendency to form slug flow.

Fig. 9(a) and (b) show the evolutions of pressure drop and void fraction with increasing heat flux under system pressures of 1.13 and 0.72 MPa, respectively. Since no experimental data of the void fraction are available, the predicted values are shown in the figures. The transition in pressure drop evolution under 1.13 MPa occurs at approximately $\alpha_v = 0.26$, which agrees well with the published criterion of the bubbly-to-slug flow transition and the transition under 0.72 MPa occurs at a lower void fraction (approximately at $\alpha_v = 0.24$). It is then supposed that the transition of bubbly-to-slug flow occurs at the transition points under both the pressure cases. Under the lower system pressure, the vapor phase has a lower density. It can be expected that the bubbles move at a larger velocity towards the axis and the peak of the radial void fraction distribution locates further away from the wall. As a result, under lower system pressure, the bubble number density in the centric area of a cross-section is larger and bubbles have a higher tendency to coalesce. This perhaps is the main reason causing the transition occurs at lower void fraction under lower system pressure.

In order to confirm that the transition point corresponds to the transition of flow regime, the differential pressure signal was analyzed. In the past decades, the pressure and differential pressure signals have been widely used as an

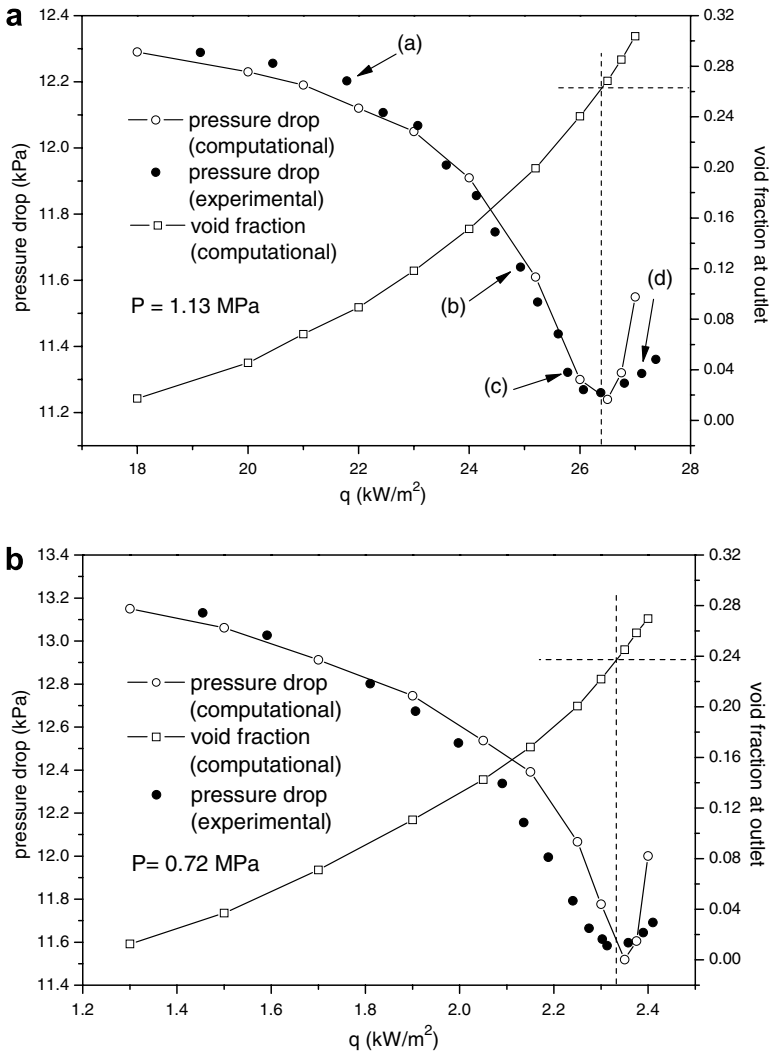

Fig. 9. Evolution of pressure drop and void fraction with increasing heat flux.

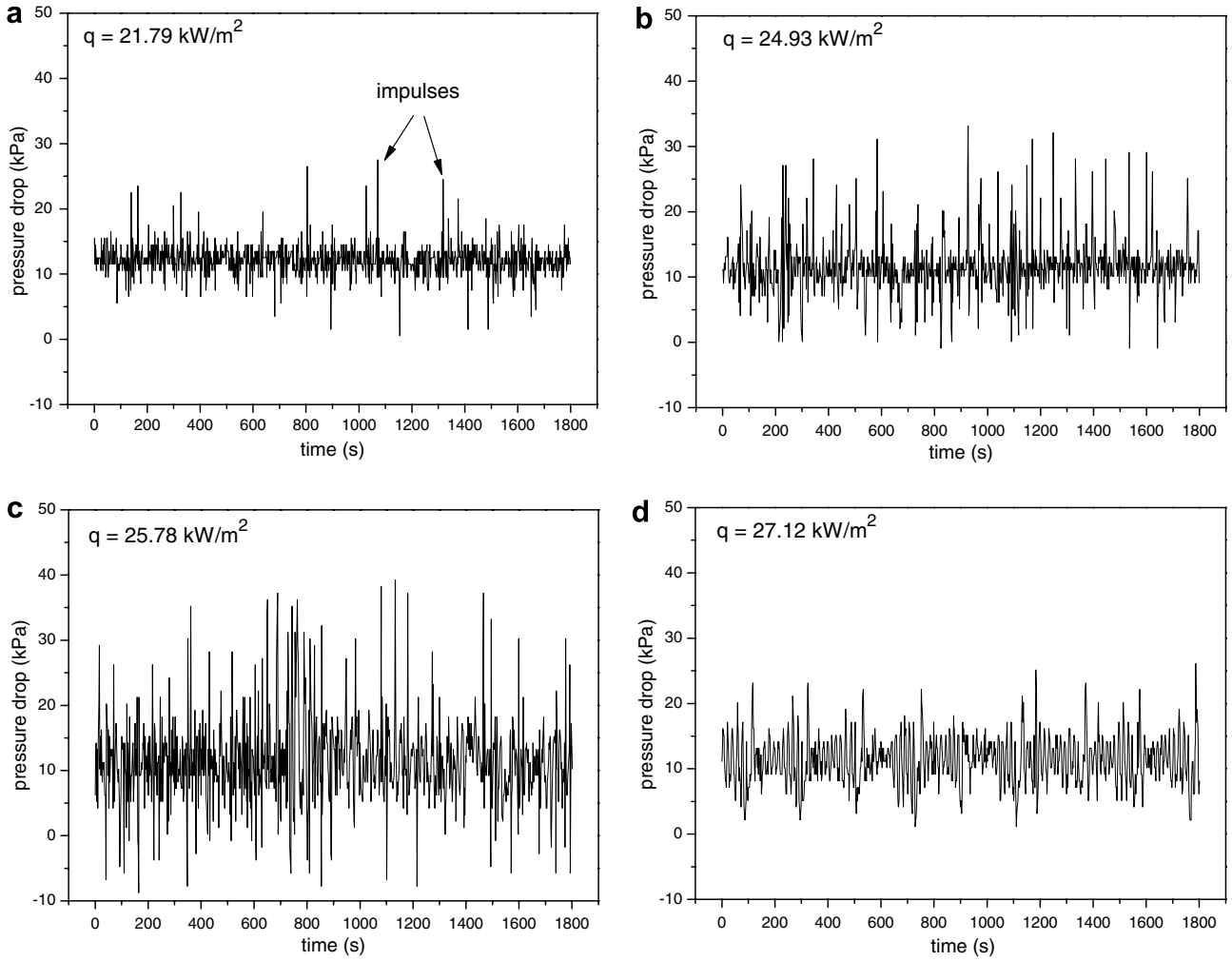

Fig. 10. Typical differential pressure signals under increasing heat flux.

accessorial method to identify flow regimes and their transitions. For example, Wambsgans [31], Tutu [32] and Matsui [33] reported their studies on flow regime identification according to pressure and differential pressure fluctuations. According to the publications, the differential pressure signals under different flow regimes have different fluctuating characteristics.

In the experimental investigations of the present study, different fluctuating characteristics are observed. Shown in Fig. 10 is the pressure drop signal of the four points (a)–(d) in Fig. 9(a). In Fig. 10, the 'impulses' are defined as the vertical long lines in the pressure drop signal and the number of impulses in a certain period of time is defined as 'impulse density'. It can be seen that both the impulse density and the impulses amplitude in the differential pressure signal increases with increased heat flux. However, as the heat flux exceeds a certain value, the impulse density begins to reduce and the fluctuation of differential pressure signal evolves in some way like a zigzag. The authors suppose that the impulse density is proportional to the number density of vapor bubbles. As the heat flux increases, more dispersed bubbles exist in the continuous liquid phase, which leads to an increasing impulse density. However, as the bubbly-to-slug flow regime transition occurs, dispersed bubbles coalesce into larger Taylor bubbles and the bubble number density decreases. Accordingly, the impulse density decreases. Similar phenomena were also observed in the experimental case of 0.72 MPa system pressure. Therefore, taking to account the void faction at the transition point and the differential pressure signals, it can be concluded that flow regime transition occurs at the transition point.

However, it seems that quantitative identification of the transition point according to differential pressure signals is difficult since the transition is gradual and there is no explicit border at the transition point. On the contrary, the numerical procedure proposed in the present study appears to be more promising.

5. Conclusions

The present study focuses on the characteristics of overall pressure drop evolution during boiling two-phase flow of LN_2 in a vertical tube, with constant mass flux and varying heat flux. Both numerical and experimental investigations were performed. The predicted pressure drop

evolution shows a satisfactory agreement with the experimental data until a reversal occurs at the transition point. The main conclusions rising from the present study are as follows.

(1) The wall lubrication force modeling has a significant effect on predicting the heat flux at which the transition occurs.
(2) Prediction of the magnitude of the pressure drop at the transition point is strongly influenced by the bubble diameter modeling.
(3) Both the theoretical analysis and the experimental evidence suggest that the transition point in the pressure drop evolution curve corresponds to the bubbly-to-slug flow regime transition.

References

[1] A. Hainoun, E. Hicken, J. Wolters, Modelling of void formation in the subcooled boiling regime in the ATHLET code to simulate flow instability for research reactors, Nucl. Eng. Des. 167 (2) (1996) 175–191.
[2] Y. Li, G.H. Yeoh, J.Y. Tu, Numerical investigation of static flow instability in a low-pressure subcooled boiling channel, Heat Mass Transfer 40 (5) (2004) 355–364.
[3] G.H. Yeoh, J.Y. Tu, Y. Li, On void fraction distribution during two-phase boiling flow instability, Int. J. Heat Mass Transfer 47 (2) (2004) 413–417.
[4] Y. Sato, K. Sekoguchi, Liquid velocity distribution in two-phase bubble flow, Int. J. Multiphas. Flow 2 (1) (1975) 79–95.
[5] X. Li, R. Wang, R. Huang, Y. Shi, Numerical investigation of boiling flow of nitrogen in a vertical tube using the two-fluid model, Appl. Therm. Eng. 26 (17–18) (2006) 2425–2432.
[6] AEA Technology plc, CFX-4.3 Solver Manual, Harwell, United Kingdom, 1999.
[7] Yu.A. Kirichenko, M.L. Dolgoy, N.M. Levchenko, et al., A study of the boiling of cryogenic liquids, Heat Transfer – Soviet Res. 8 (4) (1976) 63–72.
[8] G. Kocamustafaogullari, M. Ishii, Foundation of the interfacial area transport equation and its closure relations, Int. J. Heat Mass Transfer 38 (3) (1995) 481–493.
[9] W.B. Bald, Bubble growth constant for liquid hydrogen and liquid helium, Cryogenics 16 (12) (1976) 709–712.
[10] D.B.R. Kenning, H.D.V.M. Victor, Fully developed nucleate boiling: overlap of areas of influence and interference between bubble sites, Int. J. Heat Mass Transfer 24 (6) (1981) 1025–1032.
[11] M. Ishii, N. Zuber, Drag coefficient and relative velocity in bubbly, droplet or particulate flows, AIChE J. 25 (5) (1979) 843–855.
[12] D.A. Drew, R.T. Lahey Jr., The virtual mass and lift force on a sphere in rotating and straining inviscid flow, Int. J. Multiphas. Flow 13 (1) (1987) 113–121.
[13] N. Kurul, M.Z. Podowski, Multidimensional effects in forced convection subcooled boiling, Heat Transfer, Proceedings of the International Heat Transfer Conference, 1990, 21–26.
[14] A. Tomiyama, Struggle with computational bubble dynamics, in: Proceedings of the third International Conference on Multiphase Flow, Lyon, France, 1998.
[15] B. Koncar, I. Kljenak, B. Mavko, Modelling of local two-phase flow parameters in upward subcooled flow boiling at low pressure, Int. J. Heat Mass Transfer 47 (6–7) (2004) 1499–1513.
[16] S.P. Antal, R.T. Lahey Jr., J.E. Flaherty, Analysis of phase distribution in fully developed laminar bubbly two-phase flow, Int. J. Multiphas. Flow 17 (5) (1991) 635–652.
[17] O.E. Azpitarte, G.C. Buscaglia, Analytical and numerical evaluation of two-fluid model solutions for laminar fully developed bubbly two-phase flows, Chem. Eng. Sci. 58 (16) (2003) 3765–3776.
[18] J.Y. Tu, The influence of bubble size on void fraction distribution in subcooled flow boiling at low pressure, Int. Commun. Heat Mass Transfer 26 (5) (1999) 607–616.
[19] T.H. Lee, G.C. Park, D.J. Lee, Local flow characteristics of subcooled boiling flow of water in a vertical concentric annulus, Int. J. Multiphas. Flow 28 (8) (2002) 1351–1368.
[20] H. Anglart, O. Nylund, CFD application to prediction of void distribution in two-phase bubbly flows in rod bundles, Nucl. Eng. Des. 163 (1–2) (1996) 81–98.
[21] O. Zeitoun, M. Shoukri, Axial void fraction profile in low pressure subcooled flow boiling, Int. J. Heat Mass Transfer 40 (4) (1997) 869–879.
[22] J.Y. Tu, G.H. Yeoh, On numerical modeling of low-pressure subcooled subcooling boiling flows, Int. J. Heat Mass Transfer 45 (6) (2002) 1197–1209.
[23] M.D. Bartel, Experimental investigation of subcooled boiling, M.S.N.E. Thesis, Purdue University, West Lafayette, IN, USA, 1999.
[24] R. Situ, Y. Mi, M. Ishii, et al., Photographic study of bubble behaviors in forced convection subcooled boiling, Int. J. Heat Mass Transfer 47 (17–18) (2004) 3659–3667.
[25] K. Mishima, M. Ishii, Flow regime transition criteria for upward two-phase flow in vertical tubes, Int. J. Heat Mass Transfer 27 (5) (1984) 723–737.
[26] Y. Taitel, D. Barnea, A.E. Duckler, Modelling flow pattern transition for steady upward gas-liquid flow in vertical tubes, AIChE J. 26 (3) (1980) 345–354.
[27] D. Barnea, Transition from annular flow and from dispersed bubble flow – united models for the whole range of pipe inclinations, Int. J. Multiphas. Flow 12 (5) (1986) 733–744.
[28] S. Guet, G. Ooms, R.V.A. Oliemans, Influence of bubble size on the transition from low-Re bubbly flow to slug flow in a vertical pipe, Exp. Therm. Fluid Sci. 26 (6–7) (2002) 635–641.
[29] R. Das, S. Pattanayak, Flow regime identification in cryogenic gas-liquid flow through vertical tubes, Cryogenics 35 (6) (1995) 393–398.
[30] R. Das, S. Pattanayak, Bubble to slug flow transition in vertical upward two-phase flow of cryogenic fluids, Cryogenics 35 (7) (1995) 421–426.
[31] M.W. Wambsgans, J.A. Jandrzejczyk, M.D. France, Determination and characteristics of the transition to two-phase chug flow in small horizontal channels, AMSE J. Fluid Eng. 116 (1) (1994) 140–146.
[32] N.K. Tutu, Pressure drop fluctuations and bubble-slug transition in a vertical two-phase air-water flow, Int. J. Multiphas. Flow 10 (2) (1984) 211–216.
[33] G. Matsui, Identification of flow regimes in vertical gas–liquid two-phase flow using differential pressure fluctuations, Int. J. Multiphas. Flow 10 (6) (1984) 711–719.